H + CD_4 Abstraction Reaction Dynamics: Excitation Function and Angular Distributions†

Jon P. Camden,‡ Wenfang Hu,§ Hans A. Bechtel,‡,# Davida J. Ankeny Brown,‡ Marion R. Martin,‡ Richard N. Zare,*,‡ György Lendvay,|| Diego Troya,⊥ and George C. Schatz*,§

Department of Chemistry, Stanford University, Stanford, California 94305-5080, Department of Chemistry, Northwestern University, Evanston Illinois 60208-3113, Chemical Research Center, Hungarian Academy of Sciences, H-1525 Budapest, P.O. Box 17, Hungary, and Department of Chemistry, Virginia Tech, 107 Davidson Hall, Blacksburg, Virginia 24061-0212

Received: July 12, 2005; In Final Form: September 21, 2005

We compare experimental *photoloc* measurements and quasi-classical trajectory calculations of the integral cross sections, lab-frame speed distributions, and angular distributions associated with the CD_3 products of the H + $CD_4(\nu = 0) \rightarrow CD_3$ + HD reaction at collision energies ranging from 0.5 to 3.0 eV. Of the potential energy surfaces (PES) we explored, the direct dynamics calculations using the B3LYP/6-31G** density functional theory PES provide the best agreement with the experimental measurements. This agreement is likely due to the better overall description that B3LYP provides for geometries well removed from the minimum energy path, even though its barrier height is low by ∼0.2 eV. In contrast to previous theoretical calculations, the angular distributions on this surface show behavior associated with a stripping mechanism, even at collision energies only ∼0.1 eV above the reaction barrier. Other potential energy surfaces, which include an analytical potential energy surface from Espinosa-García and a direct dynamics calculation based on the MSINDO semiempirical Hamiltonian, are less accurate and predict more rebound dynamics at these energies than is observed. Reparametrization of the MSINDO surface, though yielding better agreement with the experiment, is not sufficient to capture the observed dynamics. The differences between these surfaces are interpreted using an analysis of the opacity functions, where we find that the wider cone of acceptance on the B3LYP surface plays a crucial role in determining the integral cross sections and angular distributions.

I. Introduction

The reaction H + CH_4 and its isotopic counterparts have been a subject of interest among experimental and theoretical chemists for decades. This reaction represents the simplest reaction occurring at a tetrahedral carbon center, and it is also important in combustion.[1] The H + $CH_4 \rightarrow CH_3 + H_2$ reaction is nearly thermoneutral [$\Delta H(0K) = -9.3 \times 10^{-4}$ eV][2] but has a large classical barrier to reaction, 0.64 eV calculated at the CCSD-(T) level with complete basis set extrapolation using CCSD-(T)/cc-pVTZ geometries. Although many experimental studies of both the forward and reverse reactions have addressed the kinetics,[3−11] the smallness of the reaction cross section has resulted in only a few experimental studies[12−14] that address the fundamental reaction dynamics, i.e., product state and angular distributions. For experimental reasons we have examined the isotopically related H + CD_4 reaction.

The reaction involves only eleven electrons, so it is amenable to high-quality ab initio calculations. As a result it has long served as a benchmark for theoretical studies of atom plus polyatomic molecule reactions.[11,15−31] Much of this work has been concerned with determination of stationary point properties and the rate constants, although occasionally there has been work on the state-resolved dynamics. Many potential energy surfaces (PES) have been developed. The most recent global surface is that obtained by Espinosa-García[27] (EG), based on the earlier Jordan and Gilbert (JG) surface[24] and using high-level ab initio calculations to determine the saddle point region of the potential surface. A more recent surface obtained by Manthe and co-workers[31] yields rate constants closer to experiment than EG, but this surface is not globally defined and thus cannot be used to describe state-resolved dynamics.

On the basis of earlier trajectory calculations[15−18] using either reduced- or full-dimensionality surfaces, the H + CD_4 reaction has long been considered to proceed through a rebound mechanism, in which the incident H atom abstracts a D at small impact parameters to give a forward-scattered CD_3. One recent experiment by Camden, Bechtel, and Zare[13] suggested that a stripping mechanism competes with the rebound mechanism. In a more recent work,[14] we compared the angular distributions from quasi-classical trajectory (QCT) to the experimental results for a center-of-mass collision energy (E_{col}) of 1.2 eV and proposed a mechanism to account for this behavior. In this paper we extend these previous studies to other collision energies to gain a deeper understanding of the H + $CD_4(\nu = 0) \rightarrow$ HD + CD_3 reaction dynamics with an emphasis on the excitation function and on product angular and speed distributions. We show that the stripping mechanism applies at energies beginning slightly above threshold. We also find that the H + CD_4 reaction is extremely sensitive to quite modest differences in the PESs. It is clear through our comparison of experiment and theory

† Part of the special issue "Donald G. Truhlar Festschrift".

* To whom correspondence should be addressed. E-mail: G.C.S., schatz@chem.northwestern.edu; R.N.Z., zare@stanford.edu.

‡ Stanford University.

§ Northwestern University.

Present address: Department of Chemistry, Massachusetts Institute of Technology, Cambridge, MA 02139.

|| Hungarian Academy of Sciences.

⊥ Virginia Tech.

10.1021/jp053827u CCC: $33.50
Published on Web 11/16/2005

that, of the surfaces examined, B3LYP provides the best description for the quantities considered here. In a separate paper[32] we discuss the product energy partitioning, which provides additional insight into the dynamics.

II. Methods and Procedures

A. Experimental Apparatus. The current experimental apparatus and the application of core-extraction time-of-flight mass spectrometry to obtain lab-frame speed distributions has been described in detail elsewhere;[33] therefore, only the primary features are described here. Hydrogen bromide (Matheson, 99.999%) or hydrogen iodide (obtained from standard synthetic procedures[34]), methane (Matheson, research grade, 99.999%), and helium (Liquid Carbonic, 99.995%) are mixed in a 1:2:4 ratio in a glass bulb. The resulting mixture is delivered to a pulsed supersonic nozzle (General Valve, Series 9, 0.6 mm orifice, backing pressure ~700 Torr) and expanded into a high vacuum chamber. The resulting molecular beam enters the extraction region of a Wiley−McLaren time-of-flight (TOF) spectrometer where it is intersected by three laser beams that initiate the reaction, detect the photolytic H atoms, and state-selectively probe the CD_3 reaction products.

Fast H atoms are generated by the UV photolysis of HBr (198−233 nm) or HI (~286 nm). For the excitation function measurements the photolytic H atoms are probed after a 5−10 ns delay using 3+1 resonance enhanced multiphoton ionization (REMPI) on the $2p\ ^2P^o \leftarrow 1s\ ^2S$ transition around 365 nm. After a time delay of 30 ns, the nascent CD_3 reaction products are state selectively ionized using a 2+1 REMPI scheme via the $3p_z\,^2A_2'' \leftarrow X\,^2A_2''$ transition[35] around 333 nm. The product ions separate according to their mass and are detected by micro-channel plates.

The 198−233 nm photolysis light is generated by frequency tripling in two BBO crystals the output of a Nd^{3+}:YAG (Continuum PL8020) pumped dye laser (Spectra Physics, PDL3). For the measurement using HI, the 286 nm light is generated by doubling in BBO the output of the same YAG and dye laser. The ~333 nm REMPI probe light is generated by frequency doubling in a BBO crystal the output of a Nd^{3+}:YAG (Spectra Physics DCR-2A) pumped dye laser (Lambda Physik, FL2002; Exciton, DCM/LDS698 mix). The H-atom probe light is generated by doubling the output of a Nd^{3+}:YAG (Continuum, PL9020) pumped dye laser (Continuum, ND6000, Exciton: LDS751) in BBO. The use of this laser setup makes it possible to independently adjust the timing between the reaction initiation (photolysis) and the probing of the H-atom reactants and CD_3 products.

The TOF mass spectrometer is operated in one of two modes. In the "crushed" mode, large extraction fields are used to collect all ions of a given mass that are formed in the focal volume of the probing laser. This mode is used for the integral cross section measurements. In "velocity-sensitive" mode, Wiley−McLaren space focusing conditions and lower extraction voltages are used to allow the $m/z = 18$ (CD_3^+) ions to separate according to their initial velocity. Furthermore, a core-extractor is used to reject ions with velocities perpendicular to the flight tube axis, thus simplifying the data analysis. A Monte Carlo simulation is used to generate an instrument response function for ions of a given initial lab-frame speed. The entire product speed range can be covered using these basis functions, which allows the measured TOF profile to be converted into a lab-frame speed distribution.

B. Experimental Excitation Function. Although it is difficult to measure absolute cross sections using the current experimental apparatus, Ayers et al.[36] described the application of the *photoloc* technique to the determination of relative excitation functions. The rate law for the formation of $[CD_3]$ is given by

$$\frac{d[CD_3]}{dt} = k[H][CD_4] \tag{1}$$

where [i] represents the concentration of species i, k is the rate constant, and t is the time delay between the photolysis and probe lasers. If we assume that the reagent concentrations are independent of time, a simple rearrangement and integration yields the concentration of the CD_3 product as a function of time:

$$[CD_3(t)] = k[H][CD_4]t = \sigma v[H][CD_4]t \tag{2}$$

where σ is the reaction cross section and v is the relative velocity of the reagents. During the course of an experiment, t and $[CD_4]$ are held constant and v can be calculated from the collision energy E. Therefore, the relative cross section is given by

$$\sigma(E) \propto \frac{[CD_3]}{[H]} \tag{3}$$

and can be determined from a measurement of the ratio $[CD_3]/[H]$ for each collision energy. We accomplish this task by successively scanning over the Q-branch members of the CD_3 $2+1\ 3p_z \leftarrow X0_0^0$ REMPI transition and the H-atom 3+1 REMPI transition.

Power laws, i.e., the dependence of the ionization efficiency as a function of the laser power, were measured for both the H and CD_3 detection lasers. For each collision energy we examined the CD_3 concentration as a function of the photolysis/probe time delay. We expect this signal to be linear until the reaction products begin to fly out of the probe laser volume, which would artificially bias our measurements toward the slower moving products in the lab frame. The signal was found to increase linearly until at least $t = 30$ ns, often longer. Figure 1 gives a representative plot of the CD_3 signal as a function of photolysis/probe delay. In this manner the CD_3 reaction products were probed at a photolysis/probe time delay of 30 ns at each collision energy.

Although the use of HI as an H-atom precursor would have extended the range over which we could make cross section measurements, only HBr was used to maintain consistency during a given experimental trial. Four collision energies

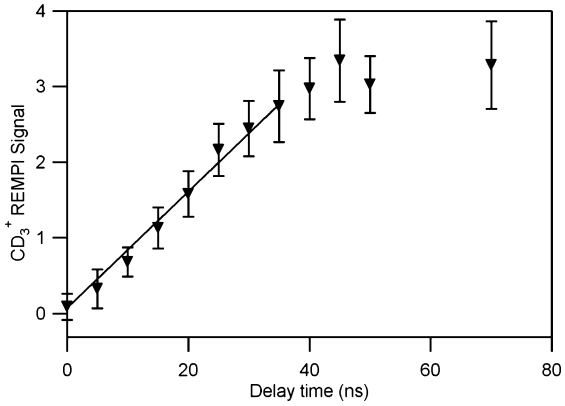

Figure 1. Reactive signal as a function of delay time between the photolysis and probe laser for the reaction $H + CD_4(v = 0) \rightarrow HD + CD_3(v = 0)$ at $E_{col} = 1.65$ eV while monitoring the $CD_3(v = 0)$ products. The signal grows linearly until about 40 ns.

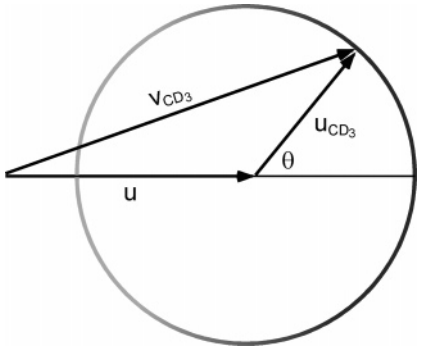

Figure 2. Newton circle for a typical *photoloc* experiment. $\vec{u}$ is the velocity of the HCD_4 center of mass, $\vec{u}_{CD_3}$ is the velocity of the CD_3 product in the center-of-mass frame, $\vec{v}_{CD_3}$ is the CD_3 lab-frame speed, and θ is the center-of-mass scattering angle measured with respect to the direction of the incident H atom.

between 1.48 and 2.36 eV were chosen. A trial consisted of scanning the methyl radical 0_0^0 Q branch and H-atom REMPI lines two times each for all collision energies. This procedure took no more than 2 h to complete, and the signal stability was checked over that time period. All scans were corrected for laser power fluctuations during the experiment according to the measured power law. The photolysis laser power was also held constant for each wavelength used and monitored during a trial. In a further attempt to avoid any experimental bias, we scanned the collision energies in a different order for each trial and measurements were taken over several days.

C. Lab-Frame Speed Distributions. The precursor molecules are expanded in a supersonic jet that cools their internal degrees of freedom and relative translations; therefore, we assume that the relative velocity of the precursor gases in the expansion is zero. For the H + $CD_4 \rightarrow CD_3$ + HD reaction the CHD_4 center-of-mass velocity vector, $\vec{u}$, is given by

$$\vec{u} = \frac{m_H}{M}\left(\frac{2E_H}{m_H}\right)^{1/2}\hat{v}_H \qquad (4)$$

where $\hat{v}_H$ is a unit vector that points in the direction of the H-atom velocity, m_H is the mass of H, E_H is the kinetic energy of H, and M is the mass of the CHD_4 system. The center-of-mass scattering angle θ is defined as the angle between the velocity of CD_3 in the center-of-mass frame $\vec{u}_{CD_3}$ and $\vec{u}$:

$$\cos\theta = \hat{u}\cdot\hat{u}_{CD_3} \qquad (5)$$

It follows that the lab-frame velocity vector of the CD_3 product is given by $\vec{v}_{CD_3} = \vec{u} + \vec{u}_{CD_3}$. Figure 2 illustrates the relationships between these vectors. The preparation and detection of a known set of reagent (H/CD_4) and product (CD_3) quantum states implies the internal energies of these fragments are known.

A photoelastic modulator (PEM-80, Hinds International Inc.) flips the direction of the photolysis laser polarization between parallel and perpendicular to the TOF axis on an every-other-shot basis to obtain the isotropic $\mathbf{I}_{iso} = I_{||} + 2I_{\perp}$ and anisotropic $\mathbf{I}_{aniso} = 2(I_{||} - I_{\perp})$ components of the core-extracted TOF profiles. The isotropic TOF profile removes any dependence on the photolysis spatial anisotropy and thus provides a direct measurement of the speed distribution. The anisotropic TOF profiles can be analyzed to estimate the amount of internal energy deposited into the coproduct by a method described in previous publications.[37,38]

Isotropic and anisotropic TOF profiles were recorded for the H + $CD_4(\nu = 0)$ reaction over the collision energy range 1.2 to 2.2 eV using both HI and HBr as a photolytic precursor; however, here we focus only on $E_{col} = 1.2$ and 1.95 eV. Figure 3 presents the CD_3 TOF profiles and the derived lab-frame speed distributions for $CD_3(\nu = 0)$ at $E_{col} = 1.2$ eV, $CD_3(\nu = 0)$ at $E_{col} = 1.95$ eV, and $CD_3(\nu_2 = 1)$ at $E_{col} = 1.95$ eV. The lowest collision energy (1.21 eV) was obtained by the photolysis of HI, whereas the 1.95 eV data used HBr as the H-atom precursor. The photodissociation of HX molecules can produce the X fragment in either its ground electronic state or spin−orbit excited state. Thus, H atoms of two different velocities are produced according to the branching ratio, [X*]/([X*] + [X]), which is a function of the dissociation wavelength. We call the H atoms coincident with X the fast channel and those coincident with X* the slow channel. The data obtained by the photolysis of HI at ∼286 nm results in a collision energy of 1.2 eV for the fast channel and 0.32 eV for the slow channel. The slow channel is significantly below the barrier to reaction and thus can be ignored. Data obtained using the photolysis of HBr at 212.8 nm ($E_{col} = 1.95$ eV) when compared to the theory are corrected for the small (∼14%) contribution of the slow channel ($E_{col} \sim 1.5$ eV). The umbrella bend excited methyl radical products [$CD_3(\nu_2 = 1)$], though constituting a minor reaction channel, are found to have the same speed distributions (Figure 3b,c) within their uncertainty.

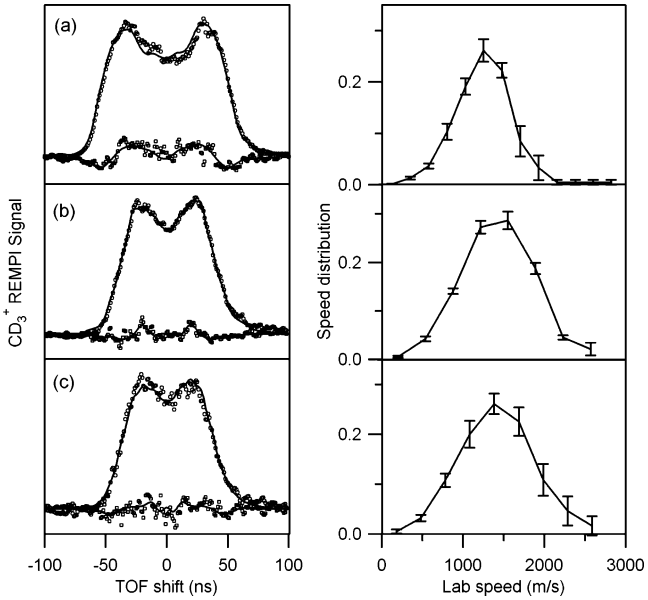

Figure 3. TOF profiles (left panel) and speed distributions (right panel) for the CD_3 products of the H + $CD_4(\nu = 0) \rightarrow$ HD + CD_3 reaction: (a) $CD_3(\nu = 0)$, $E_{col} = 1.2$ eV; (b) $CD_3(\nu = 0)$, $E_{col} = 1.95$ eV; (c) $CD_3(\nu_2 = 1)$, $E_{col} = 1.95$ eV. The TOF profiles are obtained with the probe laser on the Q branch of the 0_0^0 (a and b) or 2_1^1 (c) vibrational bands of the $2+1$ $3p_z \leftarrow$ X REMPI transition. Owing to the smaller allowed speed range for the 1.2 eV data, the TOF profile in (a) was obtained at higher resolution. The open circles are the isotropic component, the open squares are the anisotropic component, and the solid black line is the fit. The uncertainty is the 95% confidence interval derived from replicate measurements.

D. Theoretical Methods. The ground-state reaction H + CD_4 ($\nu = 0$) → HD + CD_3 has been investigated with the QCT method in conjunction with direct dynamics calculations where energy and forces are computed using electronic structure methods as the trajectory evolves. The three electronic structure models that are used include (1) density functional theory (DFT) calculations (B3LYP/6-31G**,[39,40] for which we have used the Q-Chem[41] computer program with the SG0 integration grid), (2) the MSINDO semiempirical Hamiltonian,[42−44] and (3) a reparametrized MSINDO model (hereafter referred to as "rep-

TABLE 1: Properties of the Stationary Points for the Abstraction Channel at Different Theory Levels[a,b]

SP	parameters	KGC[c]	DD[d]	QCISD(T)[e]	B3LYP	EG	JG	AM1	PM3	MSINDO[h]	reparametrized MSINDO[h]	expt[f]
CH_4	R(C−H)	1.086	1.084	1.082	1.092	1.094	1.094	1.112	1.087	1.076	1.063	1.091
	ZPE		28.6	27.8	28.3	27.3	27.2	27.9	28.5	28.7	30.1	
CH_3	R(C−H)	1.076	1.074	1.071	1.082	1.094	1.094	1.086	1.072	1.065	1.069	1.079
	ZPE		19.0	19.1	18.5	18.2	24.5	18.9	18.4	18.6	20.2	
H_2	R(H−H)		0.737	0.737	0.743	0.742	0.742	0.677	0.699	0.746	0.738	0.741
	ZPE		6.5	6.5	6.4	6.3	6.3	6.2	6.4	5.9	6.3	
TS	R(C−H)	1.082	1.080	1.077	1.087	1.094	1.094	1.110	1.086	1.077	1.078	
	R(C−H′)	1.393	1.405	1.409	1.412	1.331[g]	1.327	1.130	1.101	1.272	1.327	
	R(H′−H")	0.897	0.872	0.869	0.894	0.931[g]	0.916	1.285	1.412	0.932	0.834	
	∠HCH′	103.7	103.0	102.7	103.4	107.4	107.4	varies	varies	107.1	106.0	
	∠CH′H"	180	180	180	180	180	180	162	139	180	180	
	normal mode	3229		3297	3244	3097	3094	3193	3283	3271	3577	
	frequency	3229		3297	3243	3097	3094	3112	3209	3267	3577	
		3083		3148	3096	2962	2960	3110	3196	3082	3208	
		1763		1992	1899	1533	1601	2772	2988	1424	2498	
		1458		1468	1451	1439	1438	1398	1435	1424	1401	
		1458		1468	1445	1439	1438	1397	1429	1411	1400	
		1124		1144	1165	1264	1244	1372	1354	1367	1335	
		1124		1144	1165	1264	1244	1351	1341	1120	1071	
		1093		1073	1087	1219	1204	1345	1321	1115	1043	
		518		554	559	604	587	146	233	407	530	
		518		554	545	604	587	91	136	407	515	
		1500i	1662i	1609i	1132i	1293i	1092i	567i	618i	2261i	720i	
	ZPE	26.6	27.2	27.4	27.0	26.5	27.3	27.6	28.5	26.2	28.8	
	ΔE_{barr}	15.3	15.1	15.6	9.4	12.9	10.9	−0.2	−6.2	28.6	15.4	11.49
			(13.7)	(15.2)	(8.1)	(12.1)	(10.9)			(26.1)	(14.1)	
	ΔE_{react}	2.7	2.8	3.4	1.9	2.8	2.8	−18.5	−24.5	−1.1	2.8	0.59
			(−0.3)	(1.1)	(−1.5)	(−0.01)				(−5.3)	(−0.8)	[−0.02]

[a] Bond lengths are in angstroms, angles are in degrees, energies are in kcal/mol, and frequencies are in cm^{-1}. [b] Values in parentheses are zero-point corrected energies. [c] Reference 50. Geometries and energies are at CCSD(T)/cc-pVQZ level. [d] Reference 51. Energies were calculated using QCISD(T)/CC at the geometries determined at the MP2(FU)/TZ+2P+f level.. See the reference for details of the basis sets used. [e] Geometries were calculated using UMP2/cc-pVTZ, and energies are at QCISD(T)/6-311G(2d,2p) level. [f] Structural data and the experimental enthalpy of reaction at 0 K in brackets are from: *JANAF Thermochemical Tables*, 3rd ed.; Chase, M. W., Jr., Davies, C. A., Downey, J. R., Frurip, D. J., McDonald, R. A., Syverud, A. N., Eds.; National Bureau of Standards: Washington, DC, 1985; Vol. 14. Activation energy and reaction enthalpy are at 300 K and from: *Evaluated Kinetic Data on Gas-Phase Hydrogen Transfer Reactions of Methyl Radicals*; Kerr, J. A., Parsonage, M. J., Eds.; Butterworth: London, 1976. [g] The values for R(C−H′) and R(H′−H″) reported in ref 27 were mistyped. We thank Prof. J. Espinosa-Garcia for confirming that our values are correct. [h] We report the vibrational frequencies as obtained using the MSINDO program. Note that the frequencies in MSINDO are scaled so that they are significantly smaller than what would correspond to the actual curvature of the potential surface.

arametrized MSINDO"), in which the values of the C and H empirical parameters in MSINDO have been adjusted for this specific reaction system. The self-consistent field (SCF) unrestricted Hartree−Fock (UHF) technique is employed in all direct dynamics and electronic structure calculations. In addition, two previously developed analytical PESs are considered. They are the JG[24] and EG[27] PESs. In almost all aspects of the dynamics, we find that results on JG and EG are sufficiently close to each other that only the results on one surface need to be presented, which we choose to be EG.

The DFT approach provides the highest level of theory used in our direct dynamics calculations. The CPU time for calculating energy gradients at each integration step, however, limits the total number of trajectories that can be run. More extensive calculations are made possible with the use of semiempirical molecular orbital methods, which allow us to look at detailed aspects of the microscopic reaction mechanisms with reduced computational cost and reasonable accuracy. In the present work, we have used MSINDO, which is a method similar to the well-known AM1[45] and PM3[46,47] methods, but with somewhat more accurate saddle point properties in the present application. The effect of reparametrization of the MSINDO Hamiltonian is also examined.

The reagent collision energies explored in our calculations range from 0.5 to 3.0 eV. For JG, EG, and MSINDO dynamical calculations, batches of 10 000 trajectories are run per collision energy. For B3LYP, we have run 10 000 trajectories at 0.75, 1.2, 1.5, and 1.95 eV, respectively, and 1000 at the other collision energies due to the tremendous computational expense involved when using this method. A standard fifth-order predictor, sixth-order corrector integration algorithm[48] is employed to propagate the equations of motion along the trajectory. The integration step for the analytical PESs and B3LYP is 10.0 au (0.24 fs), and that for the MSINDO calculations is 5.0 au. When generating the initial conditions for the polyatomic reactant, we run an intramolecular trajectory starting from the equilibrium geometry of CD_4 with kinetic energy corresponding to the zero-point energy (ZPE) in each normal mode. This trajectory is integrated to cover many internal vibrational periods, and the coordinates and momenta of atoms at each point of integration are saved. When calculating the initial conditions for collision trajectories, we sample the phase of the vibrational motion from the saved intramolecular trajectory. In other aspects, the standard classical trajectory technology is followed. We did not discard trajectories that violate the ZPE constraint.

This procedure for generating initial conditions forces every trajectory to have the same CD_4 internal energy; however, there is no guarantee that the action in each vibrational mode has the correct value for the chosen initial state. This issue was studied for H + CH_4 by Huang et al. [23] using another approach (adiabatic switching) to the define the initial conditions, and they found that a small number of trajectories could in fact have important deviations from the correct behavior. In the present application it is not possible to use a better method such as adiabatic switching to define initial conditions, so we instead use the calculated reactive threshold energies to determine the importance of zero point violation in our results.

III. Results and Discussion

A. Properties of the Potential Energy Surfaces. Table 1 compares properties of the five potential surfaces used in the

TABLE 2: Adjusted Values of Empirical Parameters in MSINDO

		ζ_s^U	ζ_p^U	ζ_s	ζ_p	$-I_s$	$-I_p$	ϵ_{1s}	τ_{1s}	K_s	K_p	k_1	k_2
original value	H	1.0060		1.1576		0.5				0.1449		0.3856	0.5038
	C	1.6266	1.5572	1.7874	1.6770	0.8195	0.3824	10.430	5.0830	0.0867	0.0478	0.4936	
adjusted value	H	0.9683		1.1559		0.6383				0.2151		0.3829	0.4827
	C	2.0258	1.4350	2.0487	1.6900	0.8849	0.4386	12.688	4.6641	0.0752	0.0445	0.5598	

dynamics calculations. Also presented are results from AM1, PM3 (for which we use GAMESS[49]), and high level ab initio calculations.[50,51] Despite the greatly overestimated reaction barrier, MSINDO predicts a transition state (TS) geometry and reaction energy noticeably closer to ab initio results than does AM1 or PM3. Reparametrization of MSINDO has been performed by fitting the QCISD(T)/6-311G(2d,2p)//UMP2/cc-pVTZ data for stationary points. The new set of parameters is listed in Table 2. We see that the reparametrized MSINDO surface improves on the original one in terms of the TS geometry, classical barrier height and reaction endoergicity. Compared to high level ab initio results, the classical barrier heights are underestimated on the JG, EG, and B3LYP PESs.[52] We also note that the B3LYP/6-31G** TS geometry agrees better with the ab initio results, having a longer C−H′ (H′ is the abstracted hydrogen atom) breaking bond, hence corresponding to a later TS than those on the other surfaces. On the basis of Polanyi's rule,[53] it is expected that, at a given total energy, for PESs with late TSs, CD_4 stretch excitation promotes reactivity more than if the same energy is placed in reagent translational motion. Indeed, our recent experiments indicate that C−H stretch excitation enhances the analogous H + CH_4-($\nu_3 = 1$, antisymmetric stretching) reaction cross section by a factor of 3.0 ± 1.5.[54]

An important property of the B3LYP, reparametrized MSINDO, and MSINDO PESs is that they contain information about the H + $CD_4 \rightarrow HCD_3$ + D exchange channel that would be extremely difficult to include in an analytical PES. Accordingly, we observe some trajectories resulting in H/D exchange. The number of trajectories resulting in H/D exchange increases with collision energy, but the cross section is too small to provide a statistically meaningful result.

B. Excitation Function. In a companion work,[32] we have examined the CD_3 product state distributions in the 1.48−2.36 eV energy range and found that (1) $CD_3(\nu = 0)$ is the dominant product channel and (2) the state distribution is unchanged over that energy range. Thus, our experimental excitation function should reflect not only the cross section for forming $CD_3(\nu = 0)$ but also the cross section summed over all CD_3 product states. Figure 4 compares the experimental relative excitation function to the theoretical calculations. We have normalized the data such that the cross section at 1.5 eV is the same value. It is clear that MSINDO does not capture the observed trend whereas B3LYP, EG, and reparametrized MSINDO are in better agreement with experiment.

Combining the relative excitation function obtained in our experiments with the absolute measurement of Germann et al.[12] at 1.5 eV we derive the absolute cross section over the 1.48−2.36 eV energy range, which is compared to the theory in Figure 5. Over the energy range considered, the calculated cross sections increase from their respective thresholds to a maximum, then either gradually decrease (the EG and B3LYP curves) or become nearly constant (the MSINDO and reparametrized MSINDO curves) at higher energies.

The threshold energies for EG and reparametrized MSINDO are both just under 0.50 eV, which is only a little below the harmonic zero point corrected barrier heights (0.52 and 0.61 eV, respectively). This provides an indication that zero point violation effects must be rather small in our simulations, which is similar behavior to what has been noted for the analogous H + H_2O reaction[55] where a more careful specification of the initial conditions can be done. It is not practical to determine the effective threshold on the B3LYP surface, but inspection of Figure 5 suggests that it is probably somewhat below the zero-point corrected barrier height (0.35 eV), again indicating some, but not serious, zero point violation.

Overall, the best agreement between experiment and theory occurs for the B3LYP results. In particular, the cross section obtained by Valentini and co-workers at 1.5 eV is 0.50 ± 0.11

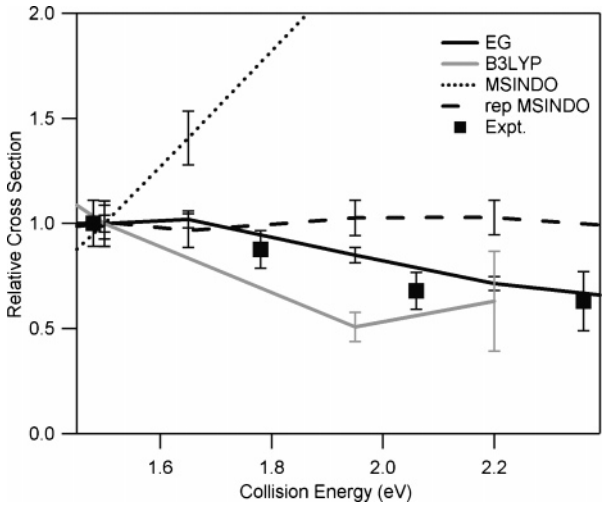

Figure 4. Comparison of the experimental and theoretical relative excitation functions for the H + $CD_4(\nu = 0) \rightarrow HD + CD_3$ reaction over the collision energy range 1.48−2.36 eV. The cross sections are normalized to 1 at $E_{col} = 1.5$ eV. The experimental uncertainty is the 95% confidence interval derived from replicate measurements.

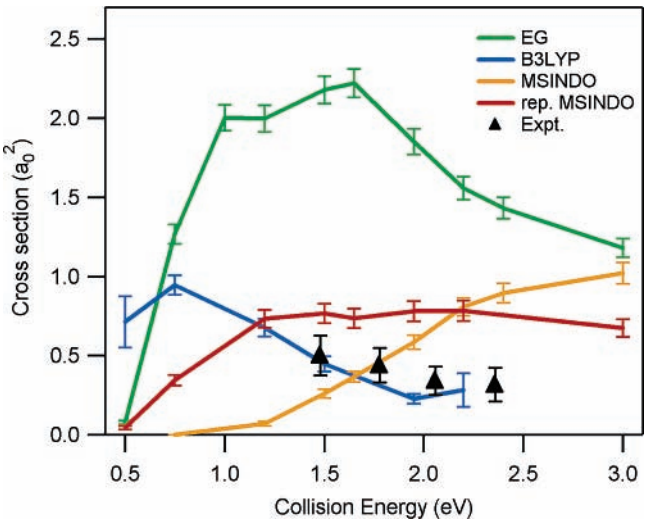

Figure 5. Comparison of the experimental and theoretical excitation functions (integral cross section vs collision energy) for the H + CD_4 $(\nu = 0) \rightarrow HD + CD_3$ reaction. The current experimental points are scaled to the absolute cross section measurement of Valentini and co-workers[12] obtained at 1.5 eV and the uncertainty takes into account the uncertainty of both the previous and current measurements.

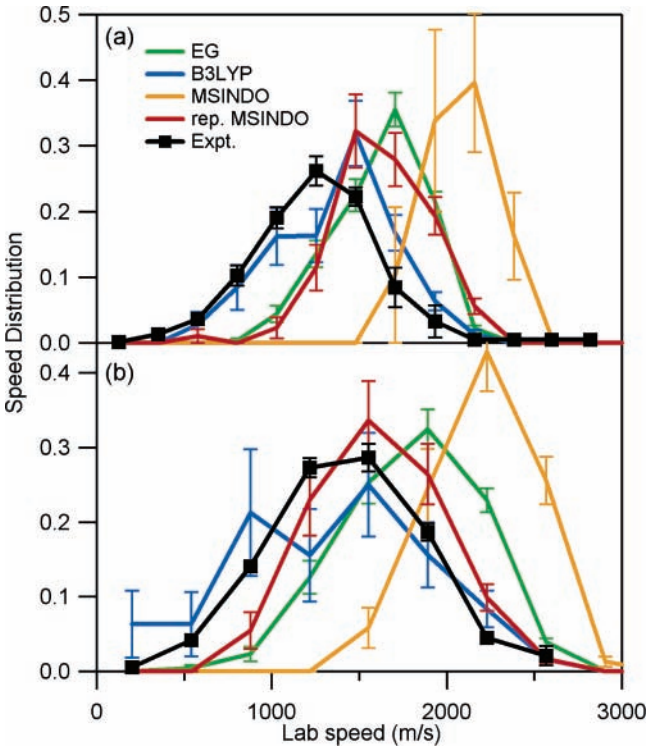

Figure 6. Experimental and theoretical CD_3 lab-speed distributions for $H + CD_4$ ($v = 0$) → $HD + CD_3$ at (a) 1.2 eV and (b) 1.95 eV. The lab-speed distribution is related to the center-of-mass scattering angle as illustrated in Figure 2.

a_0^2, whereas B3LYP gives 0.45 ± 0.05 a_0^2. The EG curve increases abruptly with increasing collision energy before 1.0 eV and reaches a peak at ~1.65 eV (~2.22 a_0^2), whereas on the B3LYP and reparametrized MSINDO surfaces the reactivity increases more slowly. The maximum on the B3LYP occurs earlier, and at higher energies the cross section remains well below that on the EG surface. The larger reactivity on the EG surface (except at very low energies) is in agreement with the nature of its TS, which is less product-like than are the B3LYP and reparametrized MSINDO TSs, and therefore more easily accessed. However, at energies close to threshold, e.g., 0.5 eV, the sequence of reactivity is B3LYP > EG ≈ reparametrized MSINDO, which reflects the reversed sequence of barrier heights on the three surfaces. Zero point violation could contribute to this result, but an additional feature favoring reaction on the B3LYP surface at low collision energies is that when the C−D-H structure bends away from collinear for geometries corresponding to the TS, the energy on B3LYP increases more slowly than on EG, providing a wider cone of acceptance.[14,56] To estimate the accuracy of our calculations, we note that the B3LYP barrier is lower than that from higher level calculations, e.g., the QCISD(T)/cc-pVTZ barrier. The latter barrier is expected to be within 0.1 eV of reality; thus, B3LYP probably underestimates the threshold to reaction, and in turn overestimates reactivity at low collision energies.

C. Lab-Frame Speed Distributions. Section II.C discussed the detailed information that is contained in the lab-frame speed distributions. The most rigorous comparison between the experiment and theory can be made by using the trajectory data to calculate purely theoretical speed distributions and compare them to the experimental distribution. This approach accounts for both the scattering angle and internal energy of the HD coproduct coincident with the observed CD_3. In Figure 6 we make such a comparison for the CD_3 lab-speed distributions at 1.2 and 1.95 eV collision energies. The 1.95 eV experiment has a small contribution that originates from the H atoms that coincide with spin−orbit excited Br atoms (quantum yield = 0.15); therefore, the theoretical distributions shown in Figure 6b are the weighted sum (according to the Br/Br* quantum yield and the calculated reaction cross sections) of the calculated speed distributions of the slow channel (1.5 eV collision energy) and the fast channel (1.95 eV). The MSINDO distributions compare poorly with the experiment, but after reparametrization we find a qualitative improvement (the reparametrized MSINDO curves), especially at 1.95 eV. The calculated distributions, however, for the reparametrized MSINDO surface are still shifted to higher speeds by several hundred m/s, and the analytical surface is also in poor agreement with the experiment. Therefore, even accounting for the large uncertainties in our calculations on the DFT PES, the B3LYP/6-31G** distributions at both energies are in general agreement with the experiment.

D. Angular Distributions. It is well-known that the speed distribution that results from a typical photoloc experiment can be converted into a differential cross section under favorable conditions.[57] Because this transformation is often poorly understood, we take this opportunity to discuss the reliability of converting the current experimental distributions to an angular distribution. In particular, we explain in detail the method used for determining the experimental differential cross section and its error in this study, using as an example our data at a collision energy of 1.2 eV.

The specific reagent and product mass combination in the $H + CD_4 \rightarrow CD_3 + HD$ reaction leads to certain advantages. Upon considering the vector diagram of Figure 2, we see that the lab speed depends on both the scattering angle and u_{CD_3}, i.e., the speed of the CD_3 product in the center of mass frame. A conversion of the lab-speed distribution to a differential cross section requires us to make a one-to-one mapping of scattering angle to lab speed. One might argue that because u_{CD_3} is determined by the amount of energy in the HD coproduct a conversion is not possible. Upon closer inspection, however, it is seen that the value of u_{CD_3} is not greatly affected by the amount of energy in the HD coproduct, so that the conversion can be done with relatively small error. For example, at a collision energy of 1.2 eV, $u_{CD_3} = 1361$ m/s when its formation is coincident with HD($E_{internal} = 0.0$ eV) and $u_{CD_3} = 1114$ m/s when coincident with HD($E_{internal} = 0.4$ eV or 33% of the total energy). We use this range of u_{CD_3} values to estimate the uncertainty in the scattering angle during the conversion of the speed distribution to a DCS. One might also argue that the upper bound we placed on the HD internal energy when calculating the error in the scattering angle is arbitrary. This impression is not the case. The lab-frame anisotropy, $\beta(v)$, can be used to determine the average energy in the unobserved HD coproduct; therefore, the experiments do provide insight into the correlated product energy partitioning. Our anisotropy measurements from the 1.2 eV TOF profile show that our choice of 0.4 eV in internal HD energy is large and likely its value is smaller, which lends further credibility to our analysis. The only way that this analysis could mislead us is if the average value of the HD internal energy distribution differs markedly from where the HD distribution has its maximum value. Such a pathological distribution runs counter to all examples and calculations and thus we feel is ruled out.

The resulting uncertainty in the cos θ coordinate caused by the HD internal energy distribution does not obscure the main trend observed in the DCS: at 1.2 eV the CD_3 products are broadly sideways scattered[14] and at 1.95 eV they are broadly sideways and backward scattered.[13] Clearly, a more detailed

TABLE 3: Calculated and Experimental Average Scattering Angles $\langle\cos\theta\rangle$ for CD_3

E_{col} (eV)	Espinosa-García PES	B3LYP/6-31G**	MSINDO	reparametrized MSINDO	ref 15 [a]	ref 17	ref 18 [a]	expt.[b]
1.08						0.87	0.26	
1.2	0.39 ± 0.02	0.09 ± 0.01	0.71 ± 0.14	0.33 ± 0.03				−0.07 ± 0.10
1.73						0.57	0.28	
1.95	0.25 ± 0.01	−0.11 ± 0.01	0.48 ± 0.04	−0.004 ± 0.0003				−0.20 ± 0.09
2.0					0.39			

[a] Refers to the hot atom reaction T + CH_4. [b] This work.

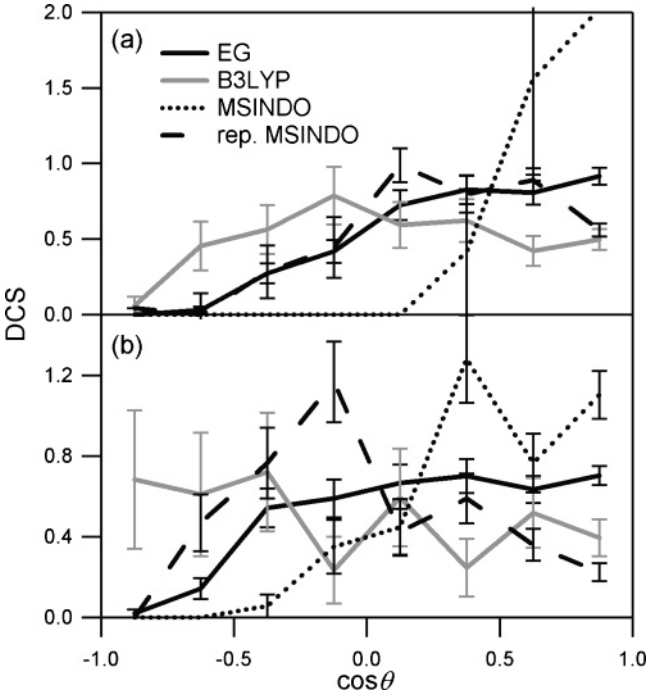

Figure 7. Calculated CD_3 angular distributions for H + CD_4 ($v = 0$) → HD + CD_3 at (a) 1.2 eV and (b) 1.95 eV expressed in terms of normalized differential cross sections $[(2\pi/\sigma)(d\sigma/d\Omega')]$.

picture of the differential cross section is desirable but it will have to await more experimental work. Still, the present analysis is able to provide a reliable estimate of the gross shape of the angular distribution.

Figure 7 compares the calculated product angular distributions for 1.2 and 1.95 eV collision energies. Table 3 summarizes the average values of the cosine of the scattering angles $\langle\cos\theta\rangle$ on the surfaces and from experiment. Previous calculated results from refs 15, 17, and 18 are also listed. For both energies the CD_3 flux is predominantly forward scattered with respect to the incident H atoms on the EG and MSINDO surfaces, contradictory to the present experiment. In fact, a markedly forward biased CD_3 angular distribution is found on the EG surface at all collision energies (Figure 8a), implying a direct reaction with a high contribution from a rebound mechanism (H atom is directed along the D−C bond and HD rebounds backward). Table 3 shows that the EG results are similar to the very old results from refs 15 and 18. The statistics on the B3LYP surface are poor, but the distribution is biased in the sideways direction at 1.2 eV, and the angular distribution switches from forward to backward with increasing collision energy (Figure 8b), indicating a change in the dominant mechanism. We can observe the same trend in the reparametrized MSINDO distributions, though they are of more forward and sideways character at low and high energies, respectively (Figure 8c).

To gain more insight into the reaction mechanism, we studied the correlation between the impact parameter b and the angular distribution on the representative EG, B3LYP, and reparametrized MSINDO surfaces (Figure 9). Collisions with $b < 1.0$ a_0 show forward scattered CD_3 at all collision energies on all three PESs. This result indicates that head-on collisions lead to backward scattered HD (rebound mechanism), as expected. In collisions with $b > 2.0$ a_0, preferred scattering changes markedly as the collision energy increases on the three surfaces. At high collision energies the CD_3 product is scattered into the backward hemisphere, whereas at energies closer to threshold the CD_3 scattering is centered around the sideways direction. The large b angular distributions agree well with the model discussed by Simpson et al.[58] for the Cl + CH_4 reaction: the backward scattered CD_3 is associated with an HD that maintains the original direction of the H atom, and corresponds to a stripping-type mechanism. As the initial relative translational energy decreases, the H atom does not have the momentum to "run away" with the D atom, and the scattering angle decreases. This type of collision also plays a special role in product energy deposition.[32]

In trying to estimate the relative contributions to the total angular distribution of small and large b collisions, we also use

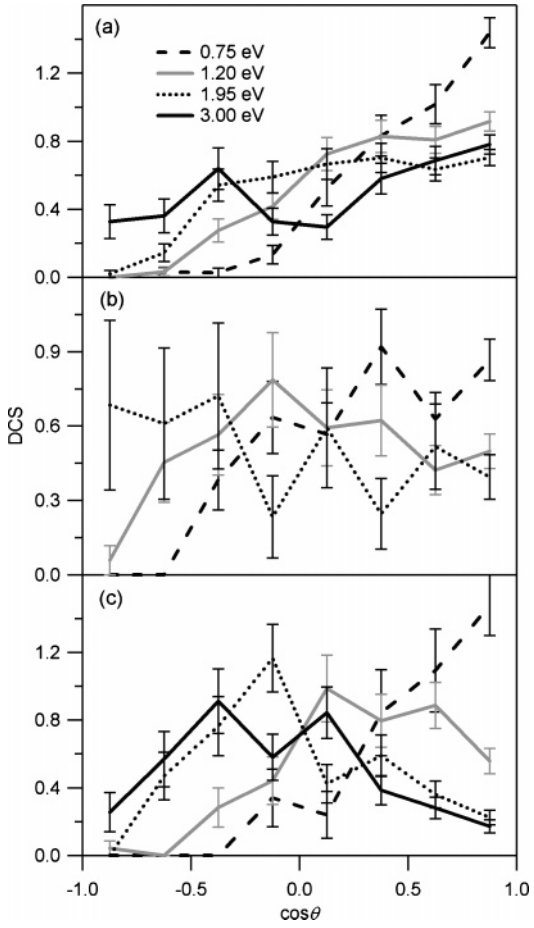

Figure 8. CD_3 angular distributions at different collision energies for the H + CD_4 ($v = 0$) → HD + CD_3 reaction on (a) the EG surface, (b) the B3LYP/6-31G** surface, and (c) the reparametrized MSINDO surface.

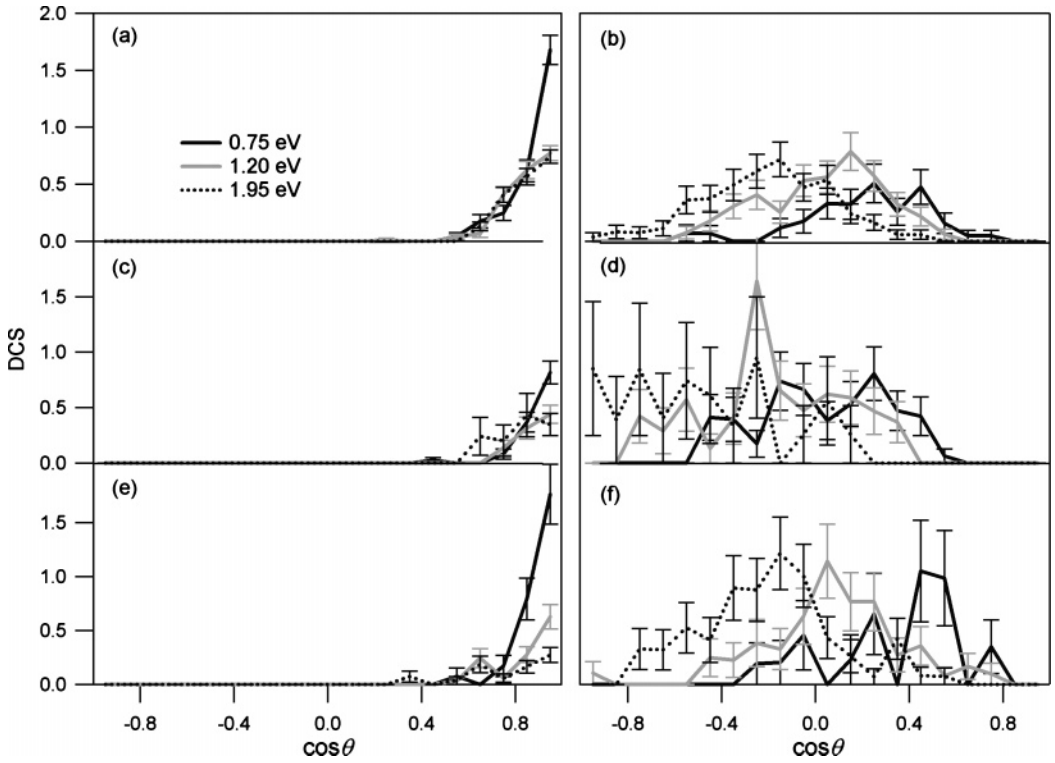

Figure 9. Dependence of the CD_3 angular distribution on the impact parameter for the $H + CD_4$ ($v = 0$) → $HD + CD_3$ reaction. Angular distributions are given for (a) the EG surface with $b < 1.0\ a_0$, (b) the EG surface with $b > 2.0\ a_0$, (c) the B3LYP/6-31G** surface with $b < 1.0\ a_0$, (d) the B3LYP/6-31G** surface with $b > 2.0\ a_0$, (e) the reparametrized MSINDO surface with $b < 1.0\ a_0$, and (f) the reparametrized MSINDO surface with $b > 2.0\ a_0$.

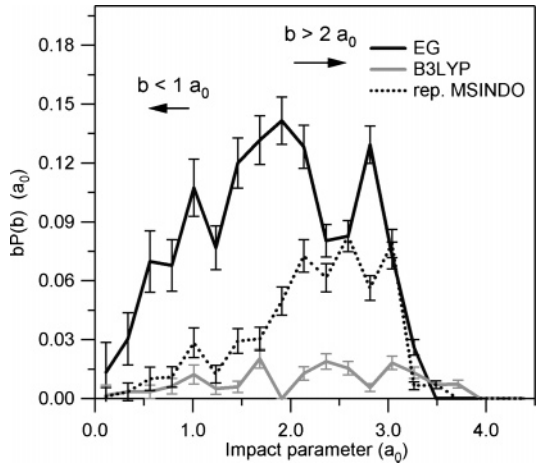

Figure 10. Opacity functions expressed as $bP(b)$ vs b for the $H + CD_4$ ($v = 0$) → $HD + CD_3$ reaction at 1.95 eV collision energy.

the calculated opacity functions to plot $bP(b)$ vs b for the three different surfaces (Figure 10). It is observed that, at a collision energy of 1.95 eV, on the EG surface the weight of small b collisions (the integration area for $b < 1.0\ a_0$) is about one-half of the weight of large b collisions ($b > 2.0\ a_0$). At the same time, the magnitude of the differential cross section (DCS) in the forward peak of the small b angular distribution is about the same as the maximum of the backward/sideways peak on the large b angular distribution (the 1.95 eV curves of Figure 9a,b). As a result, the two impact parameter regions contribute significantly to the total angular distribution, leading to a rather broad CD_3 distribution with the minimum between the forward peak arising from small b collisions and the backward/sideways peak arising from large b collisions as well as from collisions with b in the intermediate range (the 1.95 eV curve in Figure 8a). In contrast, on the B3LYP surface, the weight of small b collisions is only one-fourth of that of large b collisions (Figure 10). In addition, the magnitude of the DCSs in the backward region of the large b angular distribution is also much larger than that of the forward scattered small b angular distribution (the 1.95 eV curves of Figure 9c,d). Therefore forward scattering is negligible as compared to the contribution of large b collisions on the B3LYP surface, resulting in an angular distribution that emphasizes scattering into the backward hemisphere (the 1.95 eV curve in Figure 8b), in close agreement with experiment. On the reparametrized MSINDO surface, the contribution of small b collisions is even smaller (Figure 10, Figure 9e,f). The contribution of large b reactive collisions, which from Figure 9f we know preferentially lead to sideways scattered CD_3 at 1.95 eV, is completely dominant and biases the total angular distributions in the sideways region (the 1.95 eV curve in Figure 8c).

Clearly, the observed angular distributions can be attributed to the difference in opacity functions on the three PESs, and the opacity functions are closely related to the cones of acceptance in the saddle point region of the surfaces.[14,56] On the B3LYP and reparametrized MSINDO surfaces that have wider cones of acceptance, the contribution from sideways/peripheral reactive collisions at large impact parameters is greatly enhanced. In addition, small impact parameter nearly collinear collisions are less probable, as the flexible transition structure is less effective in "steering" the trajectory to a linear configuration as the barrier is surmounted. As a result, the wider cone of acceptance, though leading to more reactive collisions at larger impact parameters, actually results in a lower reaction probability at smaller impact parameters.

IV. Conclusion

This study compares full-dimensional quasi-classical trajectory calculations with *photoloc* experiments for the excitation

function, product speed, and angular distributions of the H + CD_4 reaction in the 0.5−3.0 eV energy range. The theoretical results are primarily derived from three potential surfaces: the analytical EG surface, density functional theory B3LYP/6-31G**, and a reparametrized MSINDO model, where the latter two involve direct dynamics calculations with the energy gradients generated on the fly.

At all energies that have been investigated, QCT calculations on the EG surface predict preferentially forward scattered methyl fragments (with respect to the incident H atom), thus corresponding to a rebound-type mechanism. On the contrary, the B3LYP and reparametrized MSINDO calculations verify a trend experimentally observed in the CD_3 distribution, which shifts from forward to backward scattering with increasing collision energy. This behavior indicates the gradually increasing importance of a stripping mechanism at higher energies. In fact, B3LYP direct dynamics calculations are found to compare quite well with experimental measurements of the reaction cross sections as well as CD_3 angular and speed distributions. This result might at first be surprising because the barrier height is ∼0.2 eV too low on B3LYP. However, it appears to better describe the surface for geometries far from the minimum energy path, which play a significant role in the product angular distributions and integral cross sections for hot atom experiments. The reparametrized MSINDO surface is shown to drastically improve over the MSINDO surface and describes the overall dynamics in qualitative agreement with experiment and the B3LYP calculations, thus providing a computationally fast option for classical trajectory calculations of specific reactions with acceptable accuracy for this degree of complexity. The present work shows that a proper description of the detailed reaction mechanism for even the simplest six-atom system as H + CD_4 is highly dependent on the quality of the PES. However, comparisons of full-dimensional theoretical calculations to state-resolved scattering experiments are now feasible for simple six-atom systems, making it possible to determine which one is the more accurate surface.

Acknowledgment. J.P.C., H.A.B, and M.R.M. thank the National Science Foundation (NSF) for graduate fellowships. The work at Stanford and Northwestern was supported by the NSF (Grant No. 0242103 and CHE-0131998, respectively). The work at Northwestern was also supported by the Air Force Office of Scientific Research through a Multidisciplinary University Research Initiative (Grant No. F49620-01-1-0335). G.L. acknowledges support from the Hungarian Academy of Sciences-Hungarian NSF collaboration (Grant No. 71) and the Hungarian NSF (Grant No. T49257).

References and Notes

(1) Warnatz, J. Rate Coefficients in the C/H/O System. In *Combustion Chemistry*; Gardiner, J., W. C., Ed.; Springer-Verlag: New York, 1984; p 197.

(2) Chase Jr., M. W.; Davies, C. A.; Downey, J. R.; Frurip, D. J.; McDonald, R. A.; Syverud, A. N. *J. Phys. Chem. Ref. Data* **1998**, *14*, Suppl. 1.

(3) Shaw, R. *J. Phys. Chem. Ref. Data* **1978**, *7*, 1179.

(4) Baulch, D. L.; Cobos, C. J.; Cox, R. A.; Esser, C.; Frank, P.; Just, T.; Kerr, J. A.; Pilling, M. J.; Troe, J.; Walker, R. W.; Warnatz, J. *J. Phys. Chem. Ref. Data* **1992**, *21*, 411.

(5) Rabinowitz, M. J.; Sutherland, J. W.; Patterson, P. M.; Klemm, B. R. *J. Phys. Chem.* **1991**, *95*, 674.

(6) Marquaire, P. M.; Dastidar, A. G.; Manthorne, K. C.; Pacey, P. D. *Can. J. Chem.* **1994**, *72*, 600.

(7) Bryukov, M. G.; Slagle, I. R.; Knyazev, V. D. *J. Phys. Chem. A* **2001**, *105*, 3107.

(8) Tsang, W.; Hampson, R. F. *J. Phys. Chem. Ref. Data* **1986**, *15*, 1087.

(9) Baeck, H. J.; Shin, K. S.; Yang, H.; Qin, Z.; Lissianski, V.; Gardner, J., W. C. *J. Phys. Chem.* **1995**, *99*, 15925.

(10) Knyazev, V. D.; Bencsura, A.; Stoliarov, S. I.; Slagle, I. R. *J. Phys. Chem.* **1996**, *100*, 11346.

(11) Sutherland, J.; Su, M.; Michael, J. *Int. J. Chem. Kinet.* **2001**, *33*, 669.

(12) Germann, G.; Huh, Y.; Valentini, J. *J. Chem. Phys.* **1992**, *96*, 1957.

(13) Camden, J. P.; Bechtel, H. A.; Zare, R. N. *Angew. Chem., Int. Ed.* **2003**, *42*, 5227.

(14) Camden, J. P.; Bechtel, H. A.; Brown, D. J. A.; Martin, M. R.; Zare, R. N.; Hu, W.; Lendvay, G.; Troya, D.; Schatz, G. C. *J. Am. Chem. Soc.* **2005**, *127*, 11898.

(15) Kuntz, P. J.; Nemeth, E. M.; Polanyi, J. C.; Wong, W. H. *J. Chem. Phys.* **1969**, *52*, 4654.

(16) Bunker, D. L.; Pattengill, M. D. *J. Chem. Phys.* **1970**, *53*, 3041.

(17) Valencich, T.; Bunker, D. L. *J. Chem. Phys.* **1974**, *61*, 21.

(18) Raff, L. M. *J. Chem. Phys.* **1974**, *60*, 2220.

(19) Chapman, S.; Bunker, D. L. *J. Chem. Phys.* **1975**, *62*, 2890.

(20) Schatz, G. C.; Wagner, A. F.; Dunning, T. H. J. *J. Phys. Chem.* **1984**, *88*, 221.

(21) Steckler, R.; Dykema, K. J.; Brown, F. B.; Hancock, G. C.; Truhlar, D. G.; Valencich, T. *J. Chem.* Phys. **1987**, *87*, 7024.

(22) Joseph, T.; Steckler, R.; Truhlar, D. G. *J. Chem. Phys.* **1987**, *87*, 7036.

(23) Huang, J.; Valentini, J. J.; Muckerman, J. T. *J. Chem. Phys.* **1995**, *102*, 5695.

(24) Jordan, M. J. T.; Gilbert, R. G. *J. Chem. Phys.* **1994**, *102*, 5669.

(25) Bowman, J. M.; Wang, D.; Huang, X.; Huarte-Larranaga, F.; Manthe, U. *J. Chem. Phys.* **2001**, *114*, 9683.

(26) Bowman, J. M. *Theor. Chem. Acc.* **2002**, *108*, 125.

(27) Espinosa-Garcia, J. *J. Chem. Phys.* **2002**, *116*, 10664.

(28) Yang, M.; Zhang, D. H.; Lee, S.-Y. *J. Chem. Phys.* **2002**, *117*, 9539.

(29) Zhang, X.; Yang, G. H.; Han, K. L.; Wang, M. L.; Zhang, J. Z. H. *J. Chem. Phys.* **2003**, *118*, 9266.

(30) Wu, T.; Manthe, U. *J. Chem. Phys.* **2003**, *119*, 14.

(31) Wu, T.; Werner, H. J.; Manthe, U. *Science* **2004**, *306*, 2227.

(32) Hu, W.; Lendvay, G.; Troya, D.; Schatz, G. C.; Camden, J. P.; Bechtel, H. A.; Brown, D. J. A.; Martin, M. R.; Zare, R. N. *J. Phys. Chem. A* **2005**, in press.

(33) Simpson, W. R.; Orr-Ewing, A. J.; Rakitzis, T. P.; Kandel, S. A.; Zare, R. N. *J. Chem. Phys.* **1995**, *103*, 7299.

(34) Schonbein, C. F. *Poggendorfs Annalen* **1849**, *78*, 516.

(35) Hudgens, J. W.; DiGiuseppe, T. G.; Lin, M. C. *J. Chem. Phys.* **1983**, *79*, 571.

(36) Ayers, J. D.; Pomerantz, A. E.; Fernandez-Alonso, F.; Ausfelder, F.; Bean, B. D.; Zare, R. N. *J. Chem. Phys.* **2003**, *119*, 4662.

(37) Simpson, W. R.; Rakitzis, T. P.; Kandel, S. A.; Orr-Ewing, A. J.; Zare, R. N. *J. Chem. Phys.* **1995**, *103*, 7313.

(38) Kim, Z. H.; Bechtel, H. A.; Zare, R. N. *J. Chem. Phys.* **2002**, *117*, 3232.

(39) Becke, A. D. *J. Chem. Phys.* **1993**, *98*, 5648.

(40) Lee, C.; Yang, W.; Parr, R. G. *Phys. Rev. B* **1988**, *37*, 785.

(41) Kong, J.; White, C. A.; Krylov, A. I.; Sherrill, C. D.; Adamson, R. D.; Furlani, T. R.; Lee, M. S.; Lee, A. M.; Gwaltney, S. R.; Adams, T. R.; Ochsenfeld, C.; Gilbert, A. T. B.; Kedziora, G. S.; Rassolov, V. A.; Maurice, D. R.; Nair, N.; Shao, Y.; Besley, N. A.; Maslen, P. E.; Dombroski, J. P.; Dachsel, H.; Zhang, W. M.; Korambath, P. P.; Baker, J.; Byrd, E. F. C.; Voorhis, T. V.; Oumi, M.; Hirata, S.; Hsu, C. P.; Ishikawa, N.; Florian, J.; Warshel, A.; Johnson, B. G.; Gill, P. M. W.; Head-Gordon, M.; Pople, J. A. *Q-Chem*, version 2.0; Q-Chem, Inc.: Export, PA, 2000.

(42) Ahlswede, B.; Jug, K. *J. Comput. Chem.* **1999**, *20*, 563.

(43) Jug, K.; Geudtner, G.; Homann, T. *J. Comput. Chem.* **2000**, *21*, 974.

(44) Bredow, T.; Geudtner, G.; Jug, K. *J. Comput. Chem.* **2001**, *22*, 89.

(45) Dewar, M. J. S.; Zoebisch, E. G.; Healy, E. F.; Stewart, J. J. P. *J. Am. Chem. Soc.* **1993**, *115*, 5348.

(46) Stewart, J. J. P. *J. Comput. Chem.* **1989**, *10*, 209.

(47) Stewart, J. J. P. *J. Comput. Chem.* **1989**, *10*, 221.

(48) Press: W. H.; Flannery, B. P.; Teukolsky, S. A.; Vetterling, W. T. *Numerical Recipes in FORTRAN: The Art of Scientific Computing*, 2nd ed.; Cambridge University Press: Cambridge, England, and New York, NY, 1992.

(49) Schmidt, M. W.; Baldridge, K. K.; Boatz, J. A.; Elbert, S. T.; Gordon, M. S.; Jensen, J. H.; Koseki, S.; Matsunaga, N.; Nguyen, K. A.; Su, S.; Windus, T. L.; Dupuis, M.; Montgomery, J. A. *J. Comput. Chem.* **1993**, *20*, 1347.

(50) Kraka, E.; Gauss, J.; Cremer, D. *J. Chem. Phys.* **1993**, *99*, 5306.

(51) Dobbs, K. D.; Dixon, D. A. *J. Phys. Chem.* **1994**, *98*, 5290.

(52) After extrapolation to the basis set and correlation energy limits,[27] a classical barrier height of 13.3 kcal/mol was obtained for the abstraction

reaction, as compared to the 15.3 kcal/mol by CCSD(T)/cc-pVQZ calculations.[50] Actually, the Espinosa-García surface was fitted to the extrapolated barrier height.

(53) Polanyi, J. C.; Wong, W. H. *J. Chem. Phys.* **1969**, *51*, 1439.

(54) Camden, J. P.; Bechtel, H. A.; Brown, D. J. A.; Zare, R. N. *J. Chem. Phys.* **2005**, *123*, 134301.

(55) Troya, D.; Gonzalez, M.; Schatz, G. C. *J. Chem. Phys.* **2001**, *114*, 8397.

(56) Low-energy collisions are expected to be strongly dependent on the features of the PESs, thus providing a test of the accuracy of these surfaces. An examination of the H−D′−C (D′ is the abstracted deuterium atom) bending-energy curves at the abstraction saddle point (these curves are generated by varying the H−D′−C angle while freezing all other coordinates at their saddle point values) reveals that the EG curve increases the fastest with the bending angle (highest anisotropy), and the modified MSINDO curve has the lowest anisotropy. The B3LYP curve, which is in good agreement with a similarly constructed curve based on QCISD(T)/6-311G(2d,2p) calculations, is intermediate between them. The lower anisotropy of a surface in the area near the TS indicates a more flexible transition structure, or a wider cone of acceptance, allowing the H−D′−C angle further from the collinear minimum energy path, thus translating into larger reaction cross sections and higher HD rotational excitation.

(57) Shafer, N. E.; Orr-Ewing, A. J.; Simpson, W. R.; Xu, H.; Zare, R. N. *Chem. Phys. Lett.* **1993**, *212*, 155.

(58) Simpson, W. R.; Rakitzis, T. P.; Kandel, S. A.; LevOn, T.; Zare, R. N. *J. Phys. Chem.* **1996**, *100*, 7938.